Published in final edited form as:
Structure. 2014 April 8; 22(4): 539–548. doi:10.1016/j.str.2014.02.006.

The Structure and Assembly Mechanism of a Novel Three-Stranded Tubulin Filament that Centers Phage DNA

Elena A. Zehr[1,3], **James A. Kraemer**[1,3], **Marcella L. Erb**[2], **Joanna K.C. Coker**[2], **Elizabeth A. Montabana**[1], **Joe Pogliano**[2], and **David A. Agard**[1,*]

[1]Department of Biochemistry and Biophysics and the Howard Hughes Medical Institute, University of California, San Francisco, San Francisco, CA 94158, USA

[2]Division of Biological Sciences, University of California, San Diego, San Diego, CA 92093, USA

SUMMARY

Tubulins are a universally conserved protein superfamily that carry out diverse biological roles by assembling filaments with very different architectures. The underlying basis of this structural diversity is poorly understood. Here, we determine a 7.1 Å cryo-EM reconstruction of the bacteriophage-encoded PhuZ filament and provide molecular-level insight into its cooperative assembly mechanism. The PhuZ family of tubulins is required to actively center the phage within infected host cells, facilitating efficient phage replication. Our reconstruction and derived model reveal the first example of a three-stranded tubulin filament. We show that the elongated C-terminal tail simultaneously stabilizes both longitudinal and lateral interactions, which in turn define filament architecture. Identified interaction surfaces are conserved within the PhuZ family, and their mutagenesis compromises polymerization *in vitro* and *in vivo*. Combining kinetic modeling of PhuZ filament assembly and structural data we suggest a common filament structure and assembly mechanism for the PhuZ family of tubulins.

INTRODUCTION

Tubulins play diverse and critical roles in eukaryotic and prokaryotic cell biology. In eukaryotes, α/β-tubulin heterodimers typically assemble into 13-protofilament microtubules required for chromosome segregation and cellular trafficking. By contrast, monomers of FtsZ facilitate septation in bacteria and archaea via protofilaments, and perhaps sheet-like structures (Lu et al., 2000; Li et al., 2007; Aylett et al., 2011), and the plasmid segregation protein TubZ from *Bacillus thuringiensis* forms 2- and 4-stranded filaments (Aylett et al., 2010) (Montabana & Agard, unpublished data). This remarkable diversity in polymer

*Correspondence: agard@msg.ucsf.edu (D.A.A).
[3]These authors contributed equally to this work

CONFLICT OF INTEREST
The authors declare that they have no conflict of interest.

architecture is mirrored by a significant divergence in protein sequence, which leads to variations in the length of loops and the presence or absence of N/C-terminal extensions (Nogales et al., 1998a; Ni et al., 2010). However, the underlying physical basis for these differences in filament structure is only poorly understood.

Despite significant divergence in primary amino acid sequences, the core fold of the tubulin/FtsZ superfamily of proteins is highly conserved. The structure consists of the nucleotide-binding N-terminal domain and the activation domain, which facilitates GTP hydrolysis via interaction of catalytic residues on the T7 loop, and H8 with the nucleotide-binding domain of the previous subunit in the filament. The two globular domains are separated by a long central helix, H7. Limited regions of strong sequence conservation are found in the loops required for GTP binding and hydrolysis, such as the G-box, the T7 loop and H8 (Nogales et al., 1998a). The divergent C-terminal tails of many tubulins are directly involved in binding associated factors and regulatory proteins (Aylett et al., 2011). Beyond these core structural elements, all tubulin homologues have a remarkably similar longitudinal (head-to-tail) mode of assembly (Nogales et al., 1998b; Lowe and Amos, 1999) that is dependent on GTP binding (Weisenberg, 1972; Bramhill and Thompson, 1994). Moreover, assembly juxtaposes the catalytic T7 loop of one subunit with the GTP exposed in the interface of the one below, whereupon stimulating its hydrolysis.

Recently a new set of tubulin-like proteins, encoded by bacteriophages, has been described (Oliva et al., 2012; Kraemer et al., 2012; Aylett et al., 2013). One of these proteins, PhuZ, from bacteriophage 201ϕ2-1 (hereafter referred to as $PhuZ_{201}$) was shown to form a highly-dynamic, spindle-like cytoskeleton within infected *Pseudomonas chlororaphis* cells that functions to both cluster and center 201ϕ2-1 phage particles at the cell midpoint. Interfering with $PhuZ_{201}$ dynamics perturbs centering and compromises phage production (Kraemer et al., 2012). $PhuZ_{201}$ belongs to the PhuZ family of tubulin homologues (Kraemer et al., 2012), encoded by the genomes of very large bacteriophages from the "ϕKZ-like viruses" genus and the phage EL (Krylov et al., 2007; Lavigne et al., 2009). Virion particles of these giant *Pseudomonas* phages (211–317 kb in size) can have heads as large as 145 nm in diameter and 200 nm tails (Fokine et al., 2007). For such large viruses, diffusion within the host cell is likely quite restricted, perhaps explaining the reliance on a tubulin cytoskeletal element.

The atomic structure of $PhuZ_{201}$ bound to GDP showed that while $PhuZ_{201}$ has a conserved tubulin/FtsZ-like fold, it possesses several unique features, including an unusually long helix H11, and an extended C-terminus. $PhuZ_{201}$ also lacks H6, which contributes to longitudinal interactions in other tubulin homologues (Kraemer et al., 2012; Nogales et al., 1999), raising questions as to how $PhuZ_{201}$ forms filaments. Though the crystal lattice appeared to contain protofilaments, adjacent longitudinal subunits were separated far more than usual, forming a "relaxed" longitudinal interface, and the vast majority of intra-protofilament interactions were derived from the interactions between the C-terminal tail and the adjacent longitudinal subunit. Highly conserved acidic residues on the C-terminal tail of one subunit (the "acidic knuckle") make electrostatic contacts with a basic patch, formed by H3, H4 and H5, of its longitudinal neighbor. The importance of these C-terminal tail interactions for filament assembly was confirmed both *in vitro* and *in vivo* by mutagenesis (Kraemer et al., 2012).

Together, these structural and functional results suggested a unique mechanism of filament assembly. Recently, atomic structures of a closely related PhuZ protein, $PhuZ_{KZ}$ (ϕKZ TubZ), encoded by the bacteriophage ϕKZ, were solved revealing a high degree of structural similarity to $PhuZ_{201}$, equivalent extensive longitudinal interactions mediated by the C-terminal tail, but with a more canonical tubulin/FtsZ "tense" longitudinal interface (Aylett et al., 2013).

In this work, we use cryo-EM to define the first high resolution three-dimensional (3D) architecture of a three-stranded tubulin filament, and use a combination of solution polymerization measurements, kinetic modeling, and mutational analyses to confirm the relevance of this architecture *in vitro* and *in vivo*, and to understand the $PhuZ_{201}$ assembly mechanism. Based on a derived pseudo-atomic model and site-directed mutagenesis, conserved charged residues within the C-terminus are identified that are essential for stabilizing three-stranded lateral interactions and filament assembly. These data allow us to propose a model for the structural origins of polymer metastability. Finally, by virtue of the high conservation of the residues that form filament contacts in $PhuZ_{201}$, we propose that the mechanism of $PhuZ_{201}$ filament assembly and its architecture are also conserved among the members of the PhuZ family.

RESULTS

$PhuZ_{201}$ assembles three-stranded filaments

To gain molecular insight into the mechanism of phage centering by $PhuZ_{201}$, we sought to determine the three-dimensional filament structure by electron microscopy (EM). While the filaments might have seemed to be two-stranded at first, the unusual pattern of regular intensities along the filament axis seen in reference-free two-dimensional (2D) class averages of negatively stained $PhuZ_{201}$ filaments is more consistent with a three-stranded architecture (Fig. 1A). These observations suggested a filament geometry distinct from that seen in the crystal (Kraemer et al., 2012). Fourier transforms of reference-free 2D averages of 500 segments of $PhuZ_{201}$ polymerized in either 1mM GTP or the slowly-hydrolysable GTP analogue, GMPCPP, looked indistinguishable, suggesting a similar filament architecture in the GDP or GTP state (Fig. 1B). As a result, and to avoid potential structural heterogeneity resulting from variability in GTP hydrolysis, the reconstruction was performed on frozen-hydrated $PhuZ_{201}$ filaments assembled in the presence of 1mM GMPCPP.

To look for complementary evidence of this unusual three-stranded organization and to gain insight into the assembly mechanism, $PhuZ_{201}$ growth kinetics were measured by right-angle light scattering at various concentrations in saturating (1 mM) GTP (Fig. 1C). Polymerization experiments were carried out in BRB80 buffer pH 7.2 to limit the formation of bundles, and the resultant critical concentration of 2.5 ± 0.1 μM was slightly lower than that previously reported for polymerization at pH 6.8 (Kraemer et al., 2012). No single step model for progression to the nucleus, defined as the minimum number of monomers assembled where polymerization is more favorable than depolymerization, fit the experimental data. Instead, a multi-step formalism derived from that developed by Flyvbjerg and colleagues (Flyvbjerg et al., 1996), where multiple subunits can come together in

multiple steps, was applied with modeling in Berkeley Madonna, a differential equation-based modeling software. The data were best described by a model wherein filaments form in two major kinetic steps: first bringing six monomers together, followed by further addition of a dimer. A nucleus size of six is consistent with a three-stranded filament, where forming two full layers would satisfy all inter-monomer contacts required for growth.

Cryo-EM in conjunction with a single particle helical analysis method (Frank et al., 1996; Egelman, 2000, 2007) was used to determine the 3D structure of the $PhuZ_{201}$-GMPCPP filament (Experimental Procedures). To better assess the resolution of the final map and to minimize overfitting, we used the "gold standard" procedure in which two separate reconstructions are independently developed from non-overlapping halves of the data and then compared at each cycle to optimize estimation of the current resolution, and filtering for the next round of parameter refinement (Scheres and Chen, 2012). The final $PhuZ_{201}$ 3D map had a conservative resolution of 7.1 Å, based on the 0.5 Fourier Shell Correlation cutoff (Fig. S1A), and had refined to the helical symmetry parameters of −116.4° rotation and 14.4 Å axial rise per subunit. The determined helical parameters were robust, as convergence to the same solution was achieved from different starting values of both helical parameters (Fig. S1B, and data not shown). While the filament is a left-handed one-start helix, the azimuthal rotation of less than −120° per subunit results in an overall right-handed supertwist (Fig. 2A). The hand of the supertwist was confirmed by tomography (data not shown). Moreover, computational experiments using different helical symmetries were done to demonstrate that all three strands were parallel (data not shown). The three-stranded architecture of the polymer is distinct from that of other cytomotive filaments characterized to date (Fig. 2B).

$PhuZ_{201}$ subunits are uniquely oriented within the filament

To interpret the cryo-EM map on a molecular level a pseudo-atomic model of the $PhuZ_{201}$ filament was built using the known atomic structure (Kraemer et al., 2012) (Fig. 2C). At the obtained resolution, although individual β-strands were not resolvable, all α-helices, many loops and the C-terminal tail (the most C-terminal 21 residues) could readily be fit, allowing unambiguous docking of the $PhuZ_{201}$ atomic model into the map. Fitting of the two globular domains and H7 separately into the map density resulted in a better fit to the map; the overall displacement was less than 1 Å suggestive of slight conformational changes within the tubulin core. However, such simplistic fitting resulted in a worse fit for a number of loops, and we felt the resolution was insufficient to justify the significant rebuilding required. Consequently, we focus here on the compromise fit, treating the entire core as a single rigid body. By contrast, the C-terminus (H11 and the C-terminal tail) required significant adjustments to fit into its corresponding cryo-EM density (Fig. S1). Particularly, the acidic knuckle (the last 13 residues of the 21 residues of the C-terminal tail) (Kraemer et al., 2012) needed to be moved together with the upper subunit, which resulted in ~6 Å displacement and 10.8° rotation of the knuckle towards the outer surface of the filament (Fig. S1C). This preserved all of the acidic knuckle interactions observed in the crystal structure (Kraemer et al., 2012). An important consequence of this movement was to prevent clashes between the knuckle with H5 of the upper subunit and H9 of a subunit in the neighboring strand. To adapt to the movement, the rest of the tail structure needed to be

repositioned towards the neighboring strand. Since the required motion was complex, a flexible fitting procedure was used (Supplemental Experimental Procedures), shifting residues F295-I302 of the tail by on average 3.5 Å towards the adjacent strand to bring them into their map density (Fig. S1D). Additionally, H11 was tilted by 6° towards the lumen to reposition it more upright within the three-stranded filament (Fig. S1E). The overall correlation coefficient between the model and the map improved from a starting value of 0.610 to 0.640 following fitting.

The model of the $PhuZ_{201}$ filament (Fig. 2C, Movie S1) revealed that the subunit orientation along the filament axis is unique with the subunit rotated by ~180° about the long axis of the filament when compared with α/β-tubulin's orientation within microtubules and TubZ subunit's orientation within the four-stranded filament (Nogales et al., 1999), (Montabana & Agard, unpublished data). Particularly, the $PhuZ_{201}$ N-terminus faces the exterior of the filament and most of the C-terminus (H11 and the C-terminal tail) faces the interior (Fig. 3A, B). The N-terminal domain defines the outer surface of the filament, whereas the lumen is dominated by the activation domain, H11 and the C-terminal tail. The acidic knuckle is largely sequestered from solvent along the axis of the filament (except for E310), but, of course, would be fully solvent-exposed at the plus end of the filament. The crescent-shaped subunits are oriented such that the curved helices H1, H2 and H3 construct the outer surface of the filament (Fig. 3A), and the straight long helices H5, H7, and H11 (Fig. 3B), surrounding the large acidic pocket left in place of the missing H6, outline the lumen. The filament is not a hollow tube, as its lumen is filled by the map densities connecting the protofilaments and the densities corresponding to the C-termini (Fig. 2B, Movie S1). The unique monomer orientation arises as a consequence of distinctive lateral interactions for a tubulin/FtsZ-like filament.

Based on the fit model, the C-terminus of each $PhuZ_{201}$ subunit contacts three other subunits: a laterally adjacent dimer as well as the adjacent longitudinal subunit (Fig. 3C). To aid in describing the unique interactions that a subunit makes within the three-stranded filament, we label subunits contacted by a subunit (#0) as follows: #1 is a longitudinally adjacent subunit within the same protofilament, #2 is a laterally adjacent subunit at the plus end and #3 is a laterally adjacent subunit at the minus end of the neighboring protofilament (Fig. 3C). As described previously, the nine, primarily charged, most distal C-terminal residues of the acidic knuckle of the subunit #0 contact subunit #1 (Kraemer et al., 2012), while at least three other contacts are formed between other residues in the C-terminal tail and residues in the subunits #2 and #3. These interactions are electrostatic/polar in nature and contribute 680 $Å^2$/subunit of buried surface area. In detail, D303 and D305 of the acidic knuckle of the subunit #0 were found to be in close proximity to K238 of H10 and R217 of H9 of the subunit #2 (Fig. 3D). Additionally, N299 of the subunit #0 seems to form a polar interface with Q157, found in the S6-H7 loop of the subunit #3, while R290 of H11 (#0) contacts E225 in the H9-S8 loop of the subunit #3 (Fig. 3D, E). The abovementioned fitting adjustments to the C-terminus were essential to make these inter-strand contacts, thereby providing insights into structural rearrangements that accompany filament formation.

Mutations to conserved residues in the predicted lateral interface disrupt $PhuZ_{201}$ filament formation

To test the validity of the predicted lateral interaction surfaces, point mutations to some of the residues were generated and mutants were tested for the ability to polymerize by right-angle light scattering, high-speed pelleting assay and negative stain EM. Based on proximity in the model, alanine mutations were made to putative salt-bridge forming residues D303, D305 within the conserved IIDXDD motif and the also well-conserved R217 (Fig. S2). Importantly, D303 and D305 were solvent-exposed in the $PhuZ_{201}$ crystal structure and consequently did not appear to be relevant for the formation of longitudinal interactions (Kraemer et al., 2012). The D303A mutation had a mild effect on $PhuZ_{201}$ assembly, with a critical concentration of 3.7 ± 0.2 μM and a slightly longer lag phase than that observed for the wild type (Table S1, Fig. 4A). The D305A mutation was more severe, with the mutant assembling at a critical concentration of 4.1 ± 0.4 μM (Table S1). The D305A assembly curve had a long lag phase and decayed soon after it reached its peak, which suggested assembly of less stable filaments (Fig. 4A). Combining these mutations had an additive effect, with the D303A/D305A double mutant polymerizing with a critical concentration of 9.4 ± 0.3 μM (Table S1), a lag phase longer than either of the single mutants, and a rising and falling polymerization curve similar to the one measured for D305A, likely indicative of polymer instability (Fig. 4A). In order to examine unstable structures the double mutant formed, it was assembled in excess GMPCPP and imaged via negative stain EM. The mutant still formed three-stranded filaments, although very rarely (Fig. S3A). By contrast, the R217A mutation resulted in no detectable polymerization measured by right-angle light scattering, even at concentrations as high as 30 μM (Fig. 4A). In the presence of GMPCPP, $PhuZ_{201}$-R217A formed only amorphous structures (Fig. S3B).

These observations supported the relevance of R217 and D305, which are predicted by the model to form a salt bridge stabilizing the lateral interface (Fig. 3D). To test this prediction, individual charge reversal mutations, R217D and D305R, along with the charge-swap double mutant, R217D/D305R, were generated, and their functional consequences examined. Similar to the R217A mutant, $PhuZ_{201}$-R217D was unable to form any detectable polymer at concentrations up to 30 μM (Fig. 4A, B), but formed amorphous structures in GMPCPP (Fig. 4C). The D305R mutant was also severely polymerization-compromised (Fig. 4A, B), with a critical concentration of 8.0 ± 0.2 μM (Table S1). The mutant no longer appeared to assemble into three-stranded filaments, but formed rare, short and twisted structures with a variable number of strands (Fig. 4D). $PhuZ_{201}$-D305R polymerized with almost no lag phase and was unstable in GTP, suggesting that the structures it formed lacked key stabilizing interactions (Fig. 4A). By contrast, combining the R217D and D305R mutations recovered polymerization (Fig. 4A, B), albeit with a significantly higher critical concentration (5.9 ± 0.3 μM) (Table S1). Importantly, the double mutant also restored formation of three-stranded filaments (Fig. 4E). These observations support the existence of a salt bridge between R217 and D305, and confirm its importance for polymer assembly.

To test whether $PhuZ_{201}$ uses the same surfaces for its assembly *in vivo*, we examined the ability of these mutant proteins to make filaments in *P. chlororaphis* cells. Fusion constructs of the wild type and the mutant versions of $PhuZ_{201}$ fused to green fluorescent protein were

generated, and conditionally expressed from a plasmid. Both the D303A and D305A mutations impaired filament formation *in vivo* (Fig. 5A, B), with the D305A single mutant and the D303A/D305A double mutant having the most severe affects. Additionally, the R217A, R217D or D305R mutants completely eliminated filament formation in cells (Fig. 5C, D). In accordance with the *in vitro* observations, the double mutant R217D/D305R resulted in a partial restoration of the ability to assemble filaments in about 15% of cells when expressed at high levels (grown in the presence of 2% arabinose) (Fig. 5C, D). Those filaments that formed were dynamic and appeared to be similar to the wild type filaments. The *in vivo* observations are completely consistent with the *in vitro* assembly behavior of the mutants, suggesting that $PhuZ_{201}$ assembles into filaments with at least three strands. These findings demonstrate the importance of the conserved residues for the establishment and stability of lateral interactions, and suggest a conserved mechanism for the filament formation within the PhuZ family of tubulin homologues.

Comparison of the filament structure to crystal structures reveals origins of twist and movement of the C-terminal tail

As demonstrated nicely by a morph (Movie S2) between the crystallographic protofilaments (3r4v and 3ZBQ) (Kraemer et al., 2012; Aylett et al., 2013) and the structure of the three-stranded filament, the $PhuZ_{201}$ dimer undergoes a striking rearrangement upon incorporation into the filament lattice. $PhuZ_{201}$ subunits form a canonical tense tubulin/FtsZ longitudinal interface in the presence of the γ-phosphate (Movie S2). Within the $PhuZ_{201}$-GMPCPP filament a subunit buries 840 $Å^2$ surface area at the tense interface as opposed to 188 $Å^2$/subunit at the relaxed interface observed within the $PhuZ_{201}$-GDP crystal (Kraemer et al., 2012) (Fig. 6A). To compare subunit packing within the filament to the post GTP-hydrolysis arrangement depicted within the $PhuZ_{KZ}$-GDP (3ZBQ) protofilament (having no twist and 43.5 Å pitch) (Aylett et al., 2013), we modeled the straight protofilament by separately superimposing two $PhuZ_{201}$ monomers over a $PhuZ_{KZ}$ longitudinal dimer using the N-terminal domains (residues 2–160 in $PhuZ_{201}$ and 4–174 in $PhuZ_{KZ}$), but excluding the activation domains and the C-termini, for alignment. The post-hydrolysis longitudinal interface in the $PhuZ_{KZ}$-like dimer model buries 930 $Å^2$/subunit. While the ~11° twist between longitudinally adjacent subunits and the slightly smaller pitch of the $PhuZ_{201}$-GMPCPP filament (43.2 Å) results in a small decrease in the longitudinal buried surface area compared to the $PhuZ_{KZ}$-like subunit packing, the overall effect is to tighten contacts around the GTP-binding pocket. Within a GMPCPP dimer the contact surface between H10 and H7 is weakened, but tighter contacts are established between the T7 and the S2-S3 loops, and the catalytic N-terminus of H8 with the T3 loop of the subunits #1 and #0 respectively (Fig. 6B). Measured distances from the catalytic Asp on the T7 loop to the β-phosphate are the same in the $PhuZ_{201}$-GMPCPP dimer and the $PhuZ_{KZ}$-like state: 6.7 Å and 6.8 Å respectively, but much shorter than in $PhuZ_{201}$-GDP (10.5 Å) (Fig. 6B).

The other significant consequence of filament formation is that both the twist and the structural rearrangement of the C-terminus contribute to the establishment of the lateral interface (Movie S2). The twist between longitudinal subunits brings the finger-like IIDXDD motif of the subunit #0 and the shape-complementary basic cavity, defined by R217 and K238, of the laterally adjacent subunit #2, ~5 Å closer towards each other.

Moreover, the C-terminus of the subunit #0 pulls away from the side of the longitudinal subunit #1 in order to form lateral interactions with the subunits #2 and #3 (Fig. 6A and Movie S2). While the majority of the contacts made by residues of the acidic knuckle remain intact, the remaining residues of the C-terminal tail and H11 (K294-D306) separate in order to establish lateral interactions (Fig. 6A). This movement shifts the C^{α} of N299 of the subunit #0 ~2 Å closer towards the C^{α} of Q157 of the subunit #3 placing the two alpha carbons ~5 Å apart. The C-terminal helix, H11, of the subunit #0 is also tilted towards the central axis of the filament to form a putative salt bridge between R290 and E225 of the subunit #3. The net result of these C-terminal tail movements is a significant loss of the intra-subunit buried surface area: 780 $Å^2$/subunit in the filament vs. 1,226 $Å^2$/subunit in the crystal (Kraemer et al., 2012) (Fig. 6A). This energetically unfavorable loss of intra-protofilament interactions is compensated by the establishment of new lateral interactions, resulting in an overall larger surface area buried per subunit in the three-stranded filament versus the crystallographic protofilament.

DISCUSSION

While the core tertiary structure is well conserved in the tubulin/FtsZ superfamily, a high degree of sequence variation, including insertions and deletions in loops and termini, leads to divergent filament morphologies. Since only the structures of microtubules and TubZ have been determined to even moderate resolution (Sui and Downing, 2010), (Montabana & Agard, unpublished data), we are just beginning to understand how these sequence variations define polymer architecture. Here, we describe the unique three-stranded filament structure of a phage-encoded tubulin homologue, $PhuZ_{201}$, at 7.1 Å resolution by cryo-EM. Docking the crystal structure of $PhuZ_{201}$-GDP (Kraemer et al., 2012) into the map reveals the critical role that the C-terminal tail plays in filament assembly. As previously noted, the acidic residues in the tail of one subunit (#0) bind to a well-defined basic pocket in the longitudinal subunit (#1) to stabilize protofilament interactions (Kraemer et al., 2012). Remarkably, the other solvent exposed acidic residues, within the conserved IIDXDD motif, are shown here to mediate lateral interactions with both #2 and #3 subunits in adjacent protofilaments. To mediate lateral contacts, the C-terminal tail undergoes a significant conformational rearrangement upon assembly, trading off intra-protofilament interactions for inter-protofilament interactions, with only the acidic knuckle retaining its original longitudinal contacts. While tubulin C-termini have been described to be involved in binding interactions with non-tubulin partners, this use of a C-terminus in defining filament architecture, leading to cooperative assembly represents a new polymerization mechanism.

Importantly, residues forming both the lateral and longitudinal contacts observed here for $nPhuZ_{201}$ are conserved in the related phage tubulins $PhuZ_{PA3}$ and $PhuZ_{KZ}$ (Fig. S2 and Fig. S4A, B). While D303, D305 and R217 are found in all three homologues, lysine (K238) is conservatively substituted for arginine in $PhuZ_{PA3}$ and $PhuZ_{KZ}$. Moreover, the putative polar interface most likely exists in $PhuZ_{PA3}$ and $PhuZ_{KZ}$ as well, since N299 and Q157 are identical or have conservative substitutions in these proteins. Finally, the putative electrostatic interface between R290 and E225 is conserved in $PhuZ_{KZ}$, and while R290 is missing in $PhuZ_{PA3}$, there is an arginine one helical turn away (R294) that could interact with E225. Thus, based on conservations of critical interactions, we propose that both

$PhuZ_{KZ}$ and $PhuZ_{PA3}$ form similar three-stranded polymers. In support of this, a 2D class average of segments from $PhuZ_{PA3}$ filaments shows a pattern characteristic of a three-stranded polymer (Fig. S4C, Fig. 1A). By contrast, the fourth, more evolutionary divergent PhuZ family homologue, $PhuZ_{EL}$, encoded by bacteriophage ϕEL that does not belong to the "ϕKZ-like viruses" genus (Lavigne et al., 2009), shows significant variations at the lateral interface, suggestive of a different filament architecture. We had also previously identified a subset of proteins (Cb, Ck, Ca and Cl) belonging to a family of *Clostridial* chromosomal tubulin homologues that also have acidic knuckle sequences (Kraemer et al., 2012). Intriguingly, these tubulins show conservation in a number of the key interactions that define the polymer contacts identified here (Fig. S2), suggesting their filament morphologies may be related.

The structural and kinetic data from this study and the three structures described in previous studies (Kraemer et al., 2012; Aylett et al., 2013) provide insight into the mechanism of PhuZ filament assembly and the role of the γ-phosphate in setting up the metastability required for filament dynamics (Fig. 7). We propose that these structures relate to distinct stages in the assembly process. First, GTP-bound monomers ($PhuZ_{KZ}$ 3ZBP) (Aylett et al., 2013) would associate via the extensive interactions between the C-terminal tail of one monomer (#0) and binding pocket of the #1 monomer forming longitudinal dimers ($PhuZ_{201}$ 3r4v) with a relaxed subunit-subunit interface (Kraemer et al., 2012). In the presence of GTP, this state is likely in equilibrium with a compacted form corresponding to a straight tense interface observed within the crystallographic protofilament ($PhuZ_{KZ}$ 3ZBQ) (Aylett et al., 2013). The linker allows the longitudinal subunit-subunit interface to elastically transition between these two states: relaxed (47Å) (Kraemer et al., 2012) and tense (~43.5 Å) (Aylett et al., 2013). Three of these dimers then laterally associate further reorganizing the C-termini, twisting and moving out their C-termini to fulfill all of the filament contacts within the hexameric nucleus. The energetically unfavorable loss of longitudinal contacts and strain from the twisting are stabilized by the newly formed lateral interactions and the presence of the γ-phosphate. The filament then grows by further addition of GTP-bound monomers and dimers. We propose that upon GTP hydrolysis, strain resulting from twisting and displacement of C-terminal interactions within each subunit is trapped by cooperative lattice interactions, leading to metastability and highly dynamic filaments.

Previous work had shown that dynamic PhuZ filaments are necessary for clustering and centering phage particles within the host bacterial cell. Interfering with filament dynamics leads to offset fragmented clusters and a significant decrease in phage burst size (Kraemer et al., 2012). Given its conservation among the members of the PhuZ family, the specific choice of a three-stranded architecture must somehow be particularly important for the viral replication cycle. One possibility is that the three-stranded filament morphology could provide a stiffer structure than the more common two-stranded architecture of plasmid-segregating prokaryotic actins in order to move such very large phage particles (200nm+) or their genomes in a crowded cytoplasm. Another intriguing possibility is that the filament's three-stranded architecture might be a structural adaptation that facilitates interactions directly, or indirectly through an adaptor protein, with three-fold symmetry centers within the capsid or tail.

There are a number of potential protein-protein interaction surfaces in PhuZ that could be functionally important. Of particular note is the acidic C-terminal tail. Within the body of the filament the tail is sequestered in the lateral interface, but it is completely exposed at the plus-end of the filament. Thus, this could provide a unique polar binding site for linkage to DNA or the phage in a manner reminiscent of the interaction between ParM filaments and the end-binding ParRC complexes that connect the filament to plasmid DNA (Garner et al., 2007; Gayathri et al., 2013). Alternatively, among the conserved surfaces exposed along the filament is an acidic patch, defined by D235, D259 and D263, that is in close proximity to the lateral interface formed by the IIDXDD motif and the basic pocket defined by R217 and K238 (Fig. S4B).

The unusual three-stranded architecture of the filament and the novel role of the C-terminus pose intriguing questions about PhuZ filament dynamics and its biological role. Although the filament structure suggests how the energy of GTP is stored within the helical lattice - through the bending of the C-terminus and the supertwist - how this structure defines the dynamic properties of the polymer remains to be explained. Future high-resolution structural studies of $PhuZ_{201}$ bound to different nucleotides, both in monomeric and filamentous forms, complemented by kinetic solution and modeling studies are needed to answer this question. Beyond this, the major issues going forward concern the physical and possible regulatory coupling of polymer dynamics to phage maturation and host cell positioning. Whether this only involves phage-encoded proteins or whether host proteins are also recruited remains to be determined.

ACCESSION CODES

The EM reconstruction and atomic coordinates have been deposited in the Electron Microscopy Data Bank, and the RCSB Protein Data Bank with accession codes EMD-5783 and 3J5V respectively.

EXPERIMENTAL PROCEDURES

Protein Expression and Purification

The genes encoding $PhuZ_{PA3}$ and $PhuZ_{201}$ were cloned into pET28a (+) with a 6-His tag on the N terminus and expressed in BL21(DE3) cells under an IPTG-inducible T7 promoter. The $PhuZ_{201}$ mutants were generated by two primer site-directed mutagenesis PCR. 1 mM IPTG was added once cells reached an OD_{600} of 0.7 at 37°C and protein was allowed to express for 8 hr at 16°C before the cells were pelleted. Cells were lysed in a buffer containing 250 mM KCl, 50 mM HEPES pH 7.4, 1 mM $MgCl_2$, 10% glycerol, 1mM DTT. EDTA-free protease inhibitor tablets were included during lysis. 250 mM imidazole was added to elute the protein from the Ni-NTA resin. The 6-His tag was cleaved overnight at 4°C by thrombin protease, followed by gel filtration chromatography (Superdex 200) in a buffer as described above, but omitting glycerol.

Negative Stain Electron Microscopy

10 μM PhuZ was polymerized in BRB80 pH7.2 with the addition of 1 mM GMPCPP for 2 min at room temperature. 4 μl of polymerized protein was applied to carbon-coated grids

after glow-discharging, unbound sample was washed away with water and grids were stained with 0.75% uranyl formate. Micrographs were collected on Tecnai T12 or T20 microscopes (FEI Co.) using accelerating voltage 120 kV or 200 kV and magnification ×52,000 or ×50,000 respectively. Images were recorded with a 4k × 4k charge-coupled device (Gatan, Inc.).

Sample Preparation and Data Collection for Cryo-Electron Microscopy

20 μM of $PhuZ_{201}$ was polymerized in 50 mM HEPES pH 8, 125 mM KCl, 5 mM $MgCl_2$, 5% glycerol and 1 mM GMPCPP for 1 minute at room temperature. 2 μl samples were applied on C-FLAT holey carbon grids and plunge-frozen into liquid ethane using Vitroblot (FEI Co.) Micrographs were collected on Technai F20 operating at 200V. Images were recorded with an 8k × 8k TemCam-F816 camera (TVIPS) at a magnification ×62,000, corresponding to a pixel size of 1.204 Å. Total electron dose was in the range of 25–30 e^- per $Å^2$ and images were acquired over an underfocus range of 0.7 to 2.5 μm.

Image Processing

CTFFIND was used to determine defocus parameters (Mindell and Grigorieff, 2003). Contrast transfer function (CTF) was corrected by applying Weiner filter to the entire micrograph. 461 cryo-EM micrographs were CTF-corrected, and 460-pixel segments with 40 pixels shift for each segment were extracted from the micrographs. The large segment size was chosen to maximize the accuracy of image alignment in the initial rounds of reconstruction. Reconstructions were determined by iterative helical real space reconstruction (IHRSR) (Egelman, 2000), performed essentially as described by Egelman *et al*, 2000, but following the “gold standard” procedure (Scheres and Chen, 2012) with two models refined independently to optimize resolution estimates and minimize data overfitting. SPIDER (Frank et al., 1996) was used for multireference alignment, projection matching, back projection and hsearch_lorentz program was used for symmetry search (Egelman, 2000). A preliminary reconstruction (reconstructed without the application of the “gold standard” procedure) of the filament starting from a plain cylinder was carried out. Then, the obtained model was low-pass filtered to 40Å and used as starting references for the reconstruction (with the application of the “gold standard” procedure) of the cryo-EM map shown in this work. Reference projections were generated at 2° intervals perpendicular to the helix axis and up to 12° out-of-plane tilt. The segments were rejected based on the excessive shifts perpendicular to the helix axis and rotations deviating from average rotations for filaments. Filaments containing less than 70% (initial rounds of alignments) or 90% (final rounds of alignment) segments determined as having the same polarity were discarded. After ten initial rounds of alignment, the segments were recentered, applying the determined in the tenth round of refinement shift values, with respect to the helix axis. Then, the segments were masked to 260 pixels along the helix axis, to minimize the effect of filament bending, and 120 pixels perpendicular to the axis with a cosine-edged mask. The initial rounds of projection matching were carried out using 2X binned data, while the final rounds were performed on unbinned images. An FSC curve was calculated between the two reconstructions at the end of each refinement round and the volumes were low-pass filtered to an estimated resolution, and then these volumes were used as the references for the next round of refinement. At the last round of refinement the half reconstructions were combined

to obtain the final cryo-EM model. A total of 69,729 unique $PhuZ_{201}$ subunits contributed to the final reconstruction. The map was low-pass filtered to 7.1 Å and sharpened with a −1200 $Å^2$ B-factor. While this is somewhat large value, even at this level of sharpening the map had very little noise. Molecular graphics and analyses were performed with UCSF Chimera (Pettersen et al., 2004). Noise in the final 3D map was eliminated for display purposes using UCSF Chimera "Hide Dust" option (Pettersen et al., 2004).

Light Scattering

Protein was thawed and spun at 80,000X RPM in a TLA100 rotor (Beckman) at 4° C prior to all light scattering assays. Right-angle light scattering was conducted by mixing $PhuZ_{201}$ with BRB80 pH 7.2 (80 mM PIPES, 1 mM $MgCl_2$, 1 mM EGTA, pH 7.2 with KOH) containing GTP using a micro-volume stopped-flow system designed in-house. An illumination wavelength of 532 nm was used. Critical concentrations were determined by plotting the maximum intensity versus $PhuZ_{201}$ concentration for each mutant. The x-intercept of this plot was used as the critical concentration.

Pelleting assay

Protein samples were spun down for 5 min at 4°C at 80,000X RPM in a TLA100 rotor (Beckman) to remove protein aggregates. 10 μM protein was polymerized in BRB80 pH 7.2, 1mM DTT and 2mM GTP for 2 min at room temperature and spun down at 80,000X RPM for 30 min at 4°C. Supernatant and pellet were analyzed by SDS-PAGE electrophoresis using 12% gel, stained with a Coomassie reagent.

Strain Construction

All mutant strains used (Table 1) were constructed via site-directed mutagenesis PCR on the previously published pME28 (Kraemer et al., 2012), which is the wild type GFP-$PhuZ_{201}$ genetic fusion borne in the broad range *Pseudomonad* vector pHERD30T (Qiu et al., 2008). *Pseudomonas chlororaphis* 200B-1 cells were prepared and transformed as in (Howard et al., 2007).

Filament Expression Levels in Mutant Strains

P. chlororaphis cells bearing the respective mutant plasmids (Table 1) were grown overnight at 30°C on a Hard Agar plate (Thomas et al., 2008) supplemented with gentamicin sulfate at 25 μg/mL. To prepare the microscope slides, agarose pads were made with 25% LB, 75% distilled H_2O, 13 mg/mL agarose, 0.1 μL/mL FM4-64 membrane dye, 0.1 μL/mL gentamicin (concentration 25 μg/mL), and the appropriate amount of arabinose. A single colony of cells was then transferred to the slide pad and incubated for 2 hours at 30°C in a humidified chamber. Images of the live cells after 2 hours of incubation were analyzed using ImageJ for total number of cells and number of cells expressing filaments at different arabinose concentrations. Cells were imaged on a Deltavision Deconvolution system (Applied Precision/GE) IX70 Olympus microscope with 100x 1.4 PlanApo lens.

Supplementary Material

Refer to Web version on PubMed Central for supplementary material.

Acknowledgments

We thank Justin Kollman and Sam Li and for invaluable discussions on image processing, Justin Kollman and Xueming Li for help with image collection, Michael Braunfeld and Bettina Keszthelyi for the help on tomography data collection and processing and Pascal Wassam for maintenance of systems hardware and software. JAK was supported by a Genetech predoctoral fellowship and an ARCS award. This work was supported by HHMI (DAA) and NIH grants GM031627 (DAA), R01GM073898 (JP), and GM104556 (JP and DAA).

References

Aylett CH, Izore T, Amos LA, Lowe J. Structure of the Tubulin/FtsZ-Like Protein TubZ from Pseudomonas Bacteriophage PhiKZ. Journal of molecular biology. 2013

Aylett CH, Lowe J, Amos LA. New insights into the mechanisms of cytomotive actin and tubulin filaments. International review of cell and molecular biology. 2011; 292:1–71. [PubMed: 22078958]

Aylett CH, Wang Q, Michie KA, Amos LA, Lowe J. Filament structure of bacterial tubulin homologue TubZ. Proceedings of the National Academy of Sciences of the United States of America. 2010; 107:19766–19771. [PubMed: 20974911]

Bramhill D, Thompson CM. GTP-dependent polymerization of Escherichia coli FtsZ protein to form tubules. Proceedings of the National Academy of Sciences of the United States of America. 1994; 91:5813–5817. [PubMed: 8016071]

Egelman EH. A robust algorithm for the reconstruction of helical filaments using single-particle methods. Ultramicroscopy. 2000; 85:225–234. [PubMed: 11125866]

Egelman EH. The iterative helical real space reconstruction method: surmounting the problems posed by real polymers. Journal of structural biology. 2007; 157:83–94. [PubMed: 16919474]

Flyvbjerg H, Jobs E, Leibler S. Kinetics of self-assembling microtubules: an “inverse problem” in biochemistry. Proceedings of the National Academy of Sciences of the United States of America. 1996; 93:5975–5979. [PubMed: 8650204]

Fokine A, Battisti AJ, Bowman VD, Efimov AV, Kurochkina LP, Chipman PR, Mesyanzhinov VV, Rossmann MG. Cryo-EM study of the Pseudomonas bacteriophage phiKZ. Structure. 2007; 15:1099–1104. [PubMed: 17850749]

Frank J, Radermacher M, Penczek P, Zhu J, Li Y, Ladjadj M, Leith A. SPIDER and WEB: processing and visualization of images in 3D electron microscopy and related fields. Journal of structural biology. 1996; 116:190–199. [PubMed: 8742743]

Garner EC, Campbell CS, Weibel DB, Mullins RD. Reconstitution of DNA segregation driven by assembly of a prokaryotic actin homolog. Science. 2007; 315:1270–1274. [PubMed: 17332412]

Gayathri P, Fujii T, Namba K, Lowe J. Structure of the ParM filament at 8.5A resolution. Journal of structural biology. 2013

Howard GT, Mackie RI, Cann IK, Ohene-Adjei S, Aboudehen KS, Duos BG, Childers GW. Effect of insertional mutations in the pueA and pueB genes encoding two polyurethanases in Pseudomonas chlororaphis contained within a gene cluster. J Appl Microbiol. 2007; 103:2074–2083. [PubMed: 18045391]

Kraemer JA, Erb ML, Waddling CA, Montabana EA, Zehr EA, Wang H, Nguyen K, Pham DS, Agard DA, Pogliano J. A phage tubulin assembles dynamic filaments by an atypical mechanism to center viral DNA within the host cell. Cell. 2012; 149:1488–1499. [PubMed: 22726436]

Krylov VN, Dela Cruz DM, Hertveldt K, Ackermann HW. “phiKZ-like viruses”, a proposed new genus of myovirus bacteriophages. Archives of virology. 2007; 152:1955–1959. [PubMed: 17680323]

Lavigne R, Darius P, Summer EJ, Seto D, Mahadevan P, Nilsson AS, Ackermann HW, Kropinski AM. Classification of Myoviridae bacteriophages using protein sequence similarity. BMC microbiology. 2009; 9:224. [PubMed: 19857251]

Li Z, Trimble MJ, Brun YV, Jensen GJ. The structure of FtsZ filaments in vivo suggests a force-generating role in cell division. The EMBO journal. 2007; 26:4694–4708. [PubMed: 17948052]

Lowe J, Amos LA. Tubulin-like protofilaments in Ca2+-induced FtsZ sheets. The EMBO journal. 1999; 18:2364–2371. [PubMed: 10228151]

Lu C, Reedy M, Erickson HP. Straight and curved conformations of FtsZ are regulated by GTP hydrolysis. Journal of bacteriology. 2000; 182:164–170. [PubMed: 10613876]

Mindell JA, Grigorieff N. Accurate determination of local defocus and specimen tilt in electron microscopy. Journal of structural biology. 2003; 142:334–347. [PubMed: 12781660]

Ni L, Xu W, Kumaraswami M, Schumacher MA. Plasmid protein TubR uses a distinct mode of HTH-DNA binding and recruits the prokaryotic tubulin homolog TubZ to effect DNA partition. Proceedings of the National Academy of Sciences of the United States of America. 2010; 107:11763–11768. [PubMed: 20534443]

Nogales E, Downing KH, Amos LA, Lowe J. Tubulin and FtsZ form a distinct family of GTPases. Nature structural biology. 1998a; 5:451–458.

Nogales E, Whittaker M, Milligan RA, Downing KH. High-resolution model of the microtubule. Cell. 1999; 96:79–88. [PubMed: 9989499]

Nogales E, Wolf SG, Downing KH. Structure of the alpha beta tubulin dimer by electron crystallography. Nature. 1998b; 391:199–203. [PubMed: 9428769]

Oliva MA, Martin-Galiano AJ, Sakaguchi Y, Andreu JM. Tubulin homolog TubZ in a phage-encoded partition system. Proceedings of the National Academy of Sciences of the United States of America. 2012; 109:7711–7716. [PubMed: 22538818]

Pettersen EF, Goddard TD, Huang CC, Couch GS, Greenblatt DM, Meng EC, Ferrin TE. UCSF Chimera--a visualization system for exploratory research and analysis. Journal of computational chemistry. 2004; 25:1605–1612. [PubMed: 15264254]

Qiu D, Damron FH, Mima T, Schweizer HP, Yu HD. PBAD-based shuttle vectors for functional analysis of toxic and highly regulated genes in Pseudomonas and Burkholderia spp. and other bacteria. Appl Environ Microbiol. 2008; 74:7422–7426. [PubMed: 18849445]

Scheres SH, Chen S. Prevention of overfitting in cryo-EM structure determination. Nature methods. 2012; 9:853–854. [PubMed: 22842542]

Sui H, Downing KH. Structural basis of interprotofilament interaction and lateral deformation of microtubules. Structure. 2010; 18:1022–1031. [PubMed: 20696402]

Thomas JA, Rolando MR, Carroll CA, Shen PS, Belnap DM, Weintraub ST, Serwer P, Hardies SC. Characterization of Pseudomonas chlororaphis myovirus 201varphi2-1 via genomic sequencing, mass spectrometry, and electron microscopy. Virology. 2008; 376:330–338. [PubMed: 18474389]

Weisenberg RC. Microtubule formation in vitro in solutions containing low calcium concentrations. Science. 1972; 177:1104–1105. [PubMed: 4626639]

Highlights

- The phage tubulin homologue, PhuZ, forms a three-stranded filament
- The extended PhuZ C-terminus defines both longitudinal and lateral contacts
- The PhuZ family of tubulins has a common filament structure and assembly mechanism

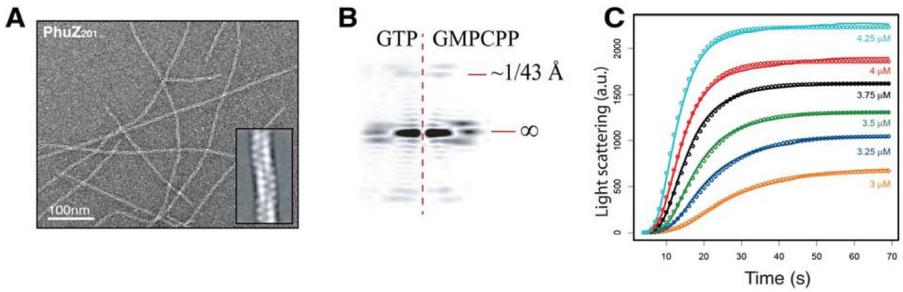

FIGURE 1. $PhuZ_{201}$ assembles three-stranded filaments and forms hexameric nucleus

(**A**) Section of a micrograph of negatively stained $PhuZ_{201}$ filaments polymerized in excess GMPCPP. Inset: reference free 2D average of 500 segments of $PhuZ_{201}$ polymer. (**B**) Fourier transforms of reference free 2D averages of 500 segments of $PhuZ_{201}$ polymerized in 1mM GTP (left) or 1mM GMPCPP (right) show that the pitch of the filament is the same and is ~43 Å. (left) GTP is hydrolyzed soon after assembly resulting in $PhuZ_{201}$-GDP filaments. (**C**) Determination of the nucleus size for $PhuZ_{201}$. $PhuZ_{201}$ was polymerized at varying concentrations in excess GTP. Solid lines are experimental data and circles are modeling results indicating a hexameric nucleus that grows by monomer and dimer addition.

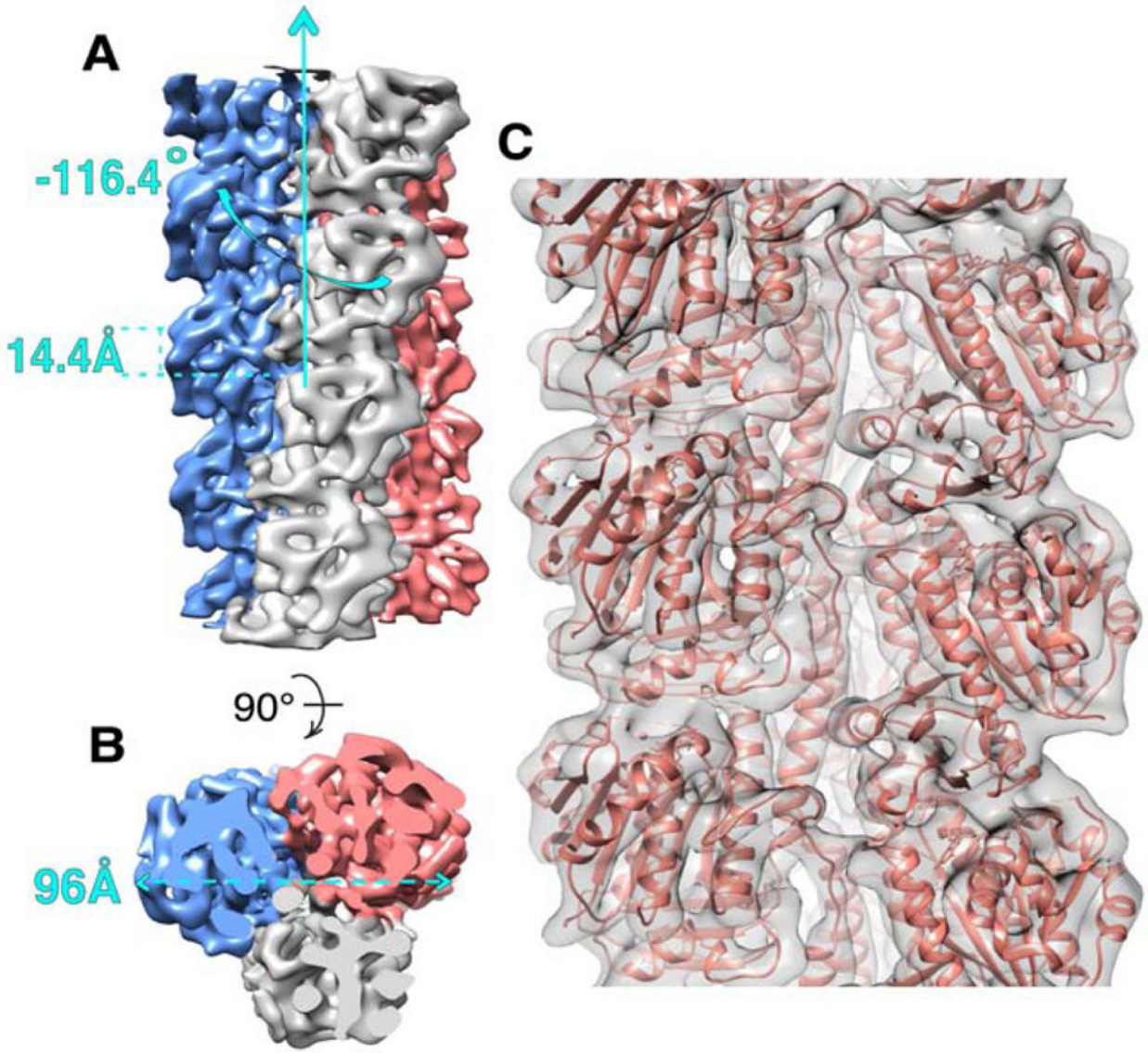

FIGURE 2. Cryo-EM map and pseudo-atomic model of $PhuZ_{201}$ filament

(**A**) and (**B**) Cryo-EM map of $PhuZ_{201}$ filament with each protofilament presented in a different color. (**A**) Map has helical symmetry of −116.4° rotation and 14.4 Å rise per subunit. (**B**) End-on view of the filament shows that it is a trimer with 96 Å diameter. (**C**) Pseudo-atomic model of $PhuZ_{201}$ filament. In gray surface is the cryo-EM density fitted with the atomic models of $PhuZ_{201}$ in salmon. See also Figure S1 and Movie S1.

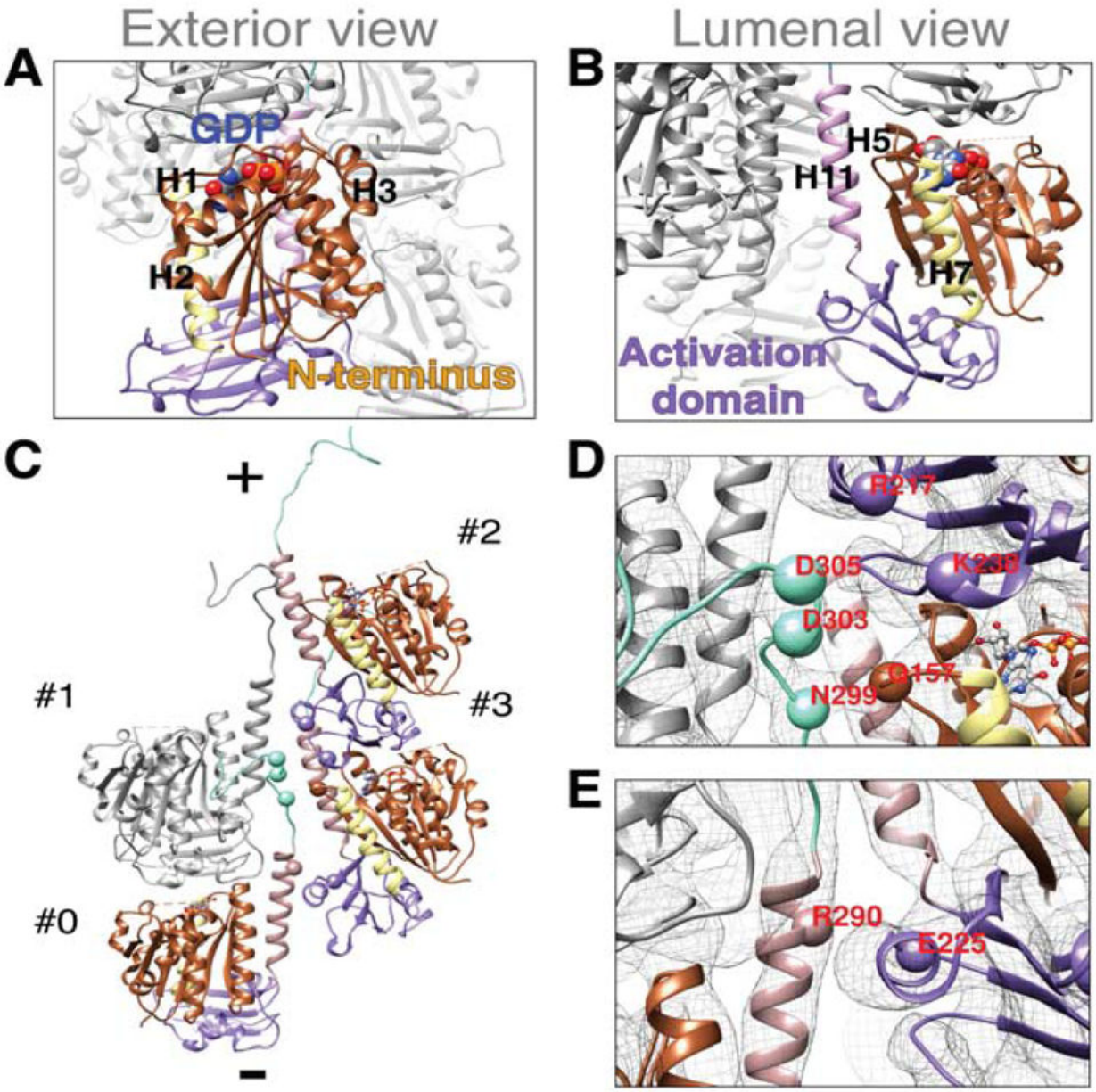

FIGURE 3. PhuZ$_{201}$ subunit is uniquely oriented within the filament and makes lateral contacts via a set of conserved residues

(**A**)–(**E**) PhuZ$_{201}$ subunit is colored by the following scheme: brown, N-terminal domain; yellow, H7; violet, activation domain; rosy brown, H11; cyan, C-terminal tail; GDP:Mg^{2+} is colored by element. Cryo-EM map density is represented as a gray mesh (**D**) and (**E**). (**A**) Exterior and **(B)** luminal views of a subunit within the filament. (**C**)–(**E**) Lateral contacts within the three-stranded filament. Alpha carbons of the residues predicted to mediate lateral contacts are shown as spheres. (**C**) C-terminus of a subunit #0 makes contacts with the longitudinal subunit #1 and with the subunits #2, and #3 of a lateral dimer. Filament ends are designated as (+) end with the C-termini and (−) end with the activation domains. (**D**) D303 and D305 of #0 contact K238 and R217 of #2 respectively; N299 of #0 contacts Q157 of #3; (**E**) R290 of #0 contacts E225 of #3. See also Figure S2.

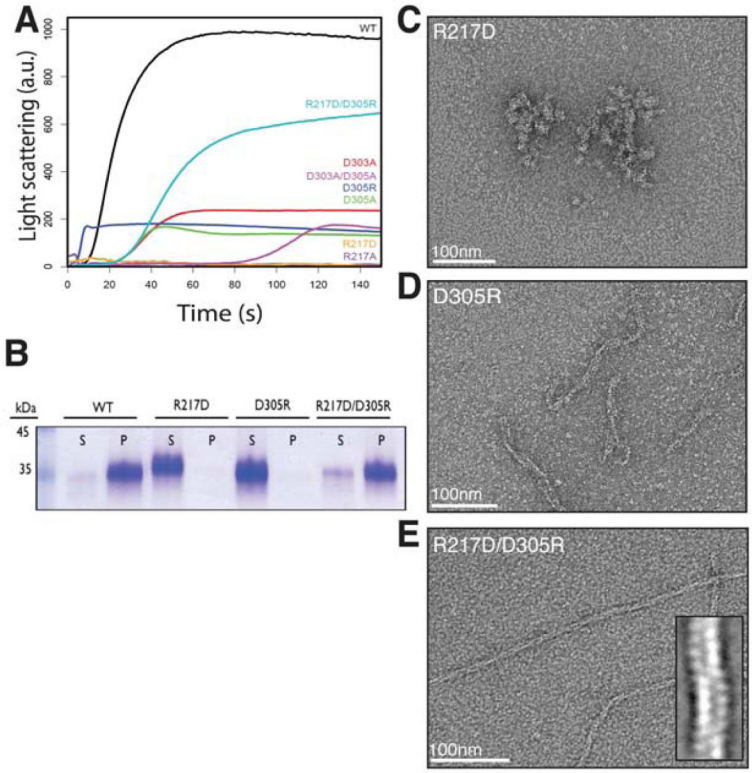

FIGURE 4. Mutations to residues predicted to mediate lateral contacts disrupt PhuZ$_{201}$ assembly *in vitro*

(**A**) Right-angle light-scattering traces of PhuZ$_{201}$ wild type (WT) and mutants polymerized in 1mM GTP. The following concentrations were used: 3 μM WT in black, 5 μM D303A in red, 7 μM D305A in green, 9 μM D305R in dark blue, 30 μM R217A in purple, 30 μM R217D in orange, 10 μM D303A/D305A in violet, and 6 μM R217D/D305R in cyan. (**B**) Polymerization of PhuZ$_{201}$ mutants in excess GTP was assayed by high-speed pelleting assay as described under "Experimental Procedures" with supernatant (S) and pellet (P) fractions analyzed by SDS-PAGE. (**A**) and (**B**) Charge reversal mutant R217D/D305R partially restores the ability to form filaments. (**C**)–(**E**) Sections of micrographs of negatively stained PhuZ$_{201}$ mutants polymerized in excess GMPCPP. PhuZ$_{201}$ single mutants R217D (**C**) and D305R (**D**) are unable to form three-stranded filaments, but the double mutant R217D/D305R (**E**) assembles three-stranded filaments (inset). See also Table S1 and Figure S3.

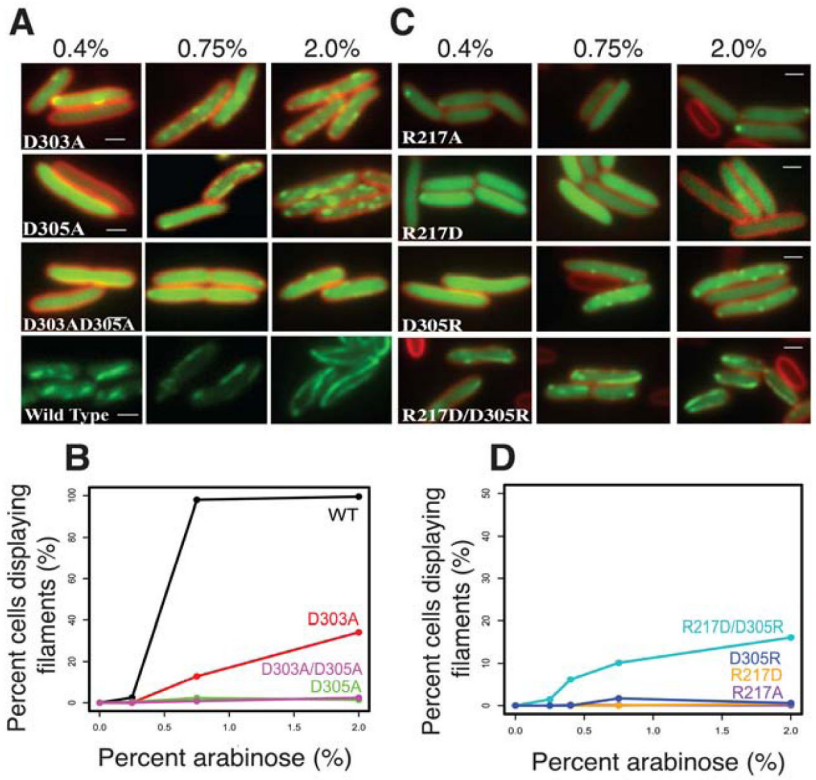

FIGURE 5. PhuZ$_{201}$ assembles via the same set of lateral surfaces *in vivo* as *in vitro*

(**A**) and (**C**) Fluorescent micrographs of uninfected *P. chlororaphis* cells expressing various GFP-PhuZ$_{201}$ mutant constructs. (**A**) Shown are the three tail mutants D303A, D305A and the double mutant D303A/D305A at 0.4%, 0.75%, and 2% arabinose induction. Wild type PhuZ$_{201}$ is in the last strip for comparison. All mutants have compromised filament formation. (**B**) Quantitation of data in (**A**) indicating that of the three mutants, only D303A shows any appreciable polymerization at 2% arabinose. (**C**) Shown are the four tail mutants R217A, R217D, D305R and the double mutant R217D/ D305R at 0.4%, 0.75% and 2% arabinose induction. The single mutants are unable to make filaments, but the charge reversal in the double mutant partially restores filament formation. (**D**) Quantitation of the concentration data from (**C**). All scale bars = 1 micron.

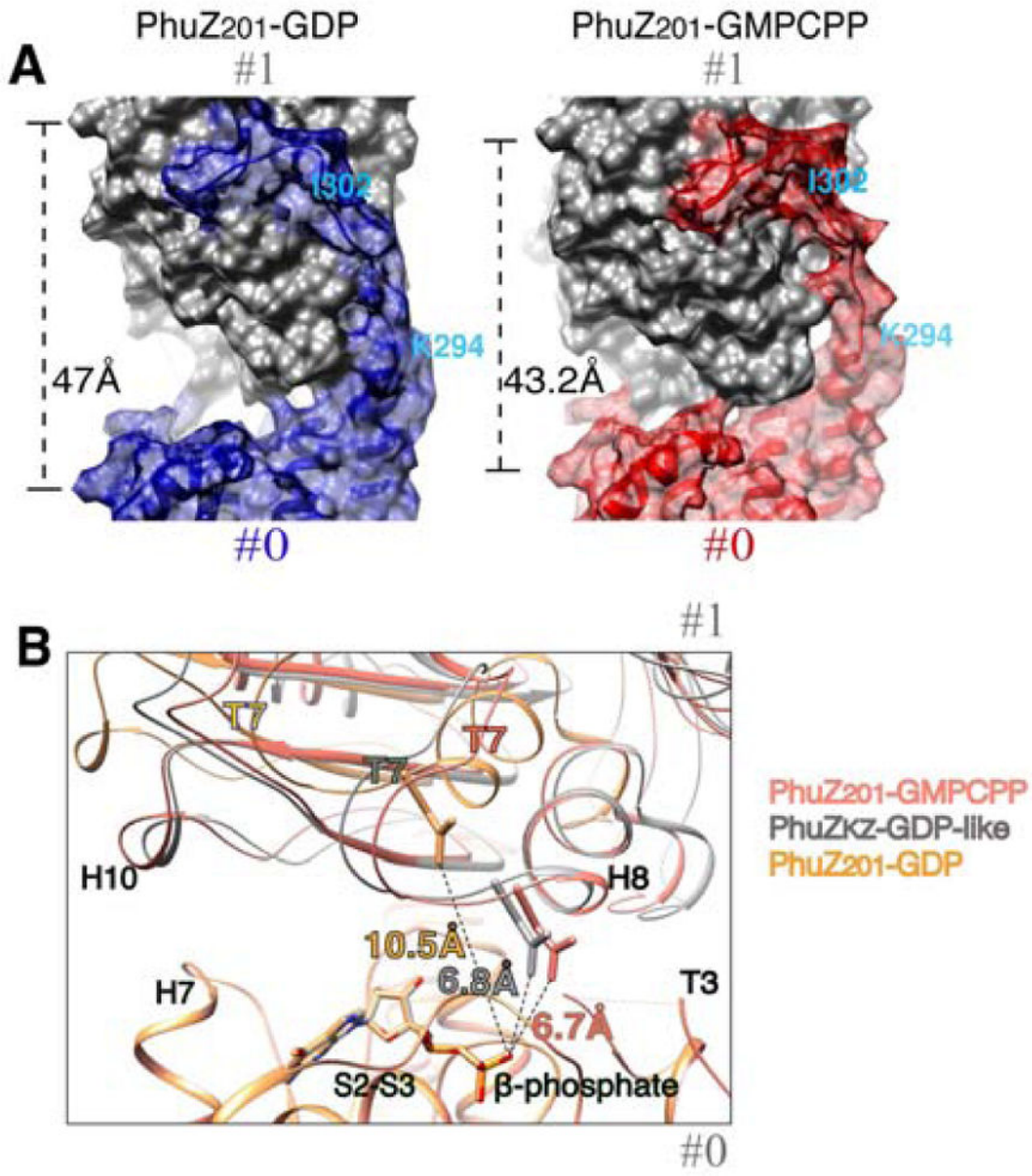

FIGURE 6. Comparison of the longitudinal packing between $PhuZ_{201}$-GDP, $PhuZ_{KZ}$-like-GDP and the three-stranded filament

(A) and **(B)** Longitudinal subunits within a dimer are labeled as #0 and #1. (**A**) $PhuZ_{201}$ dimers representative of the packing within the crystal (3r4v) (Kraemer et al., 2012) (left) vs the three-stranded filament (right) are shown as molecular surfaces. (left) $PhuZ_{201}$ subunit packing within the crystal: the C-terminal tail of the subunit #0 in blue forms extensive interactions with the side of the subunit #1 in gray. The dimer has a relaxed longitudinal interface with 47 Å spacing. (right) $PhuZ_{201}$ subunit packing within the three-stranded filament: the C-terminal tail of the subunit #0 in red forms weak longitudinal contacts with the side of the subunit #1 in gray. The dimer has a tense canonical tubulin/FtsZ longitudinal interface with 43.2 Å spacing. (**B**) Magnified view of the longitudinal interfaces in: $PhuZ_{201}$-GMPCPP dimer in salmon, $PhuZ_{201}$ mimicking subunit packing as in a $PhuZ_{KZ}$-GDP dimer (3ZBQ) (Aylett et al., 2013) in gray and a $PhuZ_{201}$-GDP dimer (3r4v) (Kraemer et al., 2012) in yellow. The dimers were superimposed via the residues (2–271) corresponding to the N-terminal domains and the activation domains,

but excluding the residues corresponding to the C-termini, of the subunits at minus ends. Measured distances from the catalytic Asp on the T7 loop to the β-phosphate are: 6.7 Å the three-stranded filament, 6.8 Å in $PhuZ_{KZ}$-GDP-like state, and 10.5 Å in $PhuZ_{201}$-GDP. See also Movie S2.

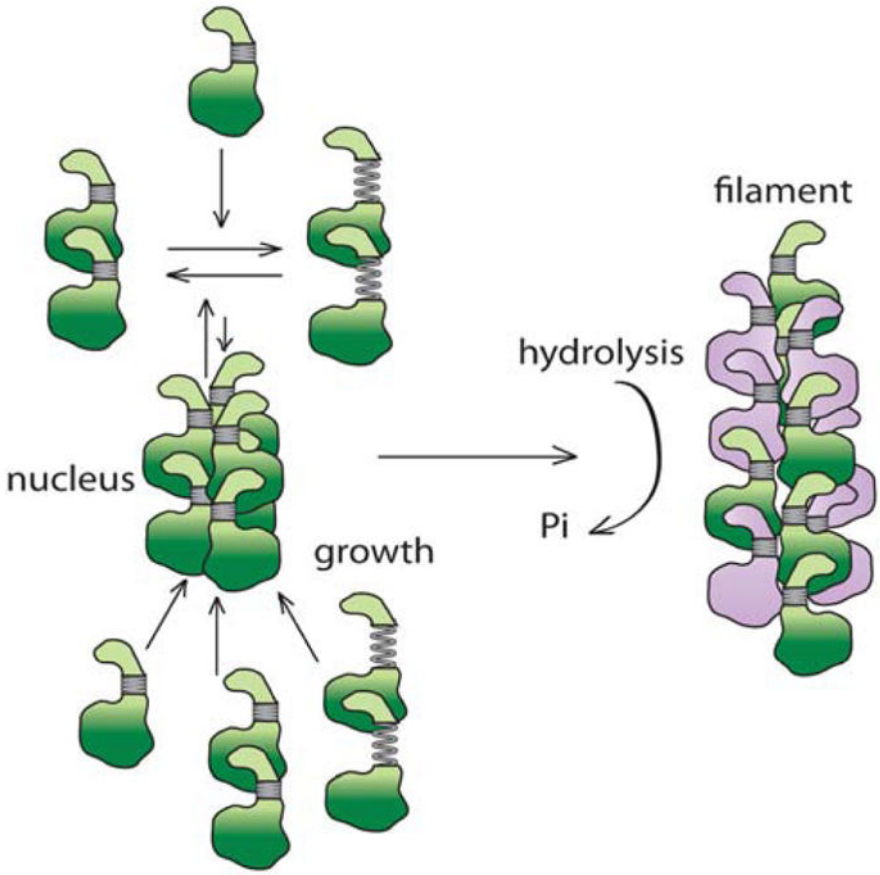

FIGURE 7. Model for PhuZ assembly

GTP-bound PhuZ is in green and GDP-bound is in purple. PhuZ monomers as seen in the crystal (3ZBP) (Aylett et al., 2013) assemble dimers with a tense longitudinal interface as in the crystal structure (3ZBQ) (Aylett et al., 2013) or the relaxed interface as in the crystal structure (3r4v) (Kraemer et al., 2012). Three dimers form a hexameric nucleus with subunits displaying the intramolecular contacts as seen in the pseudo-atomic model described in this work. The nucleus grows by the addition of dimers and monomers. GTP is hydrolyzed soon after filament assembly.

Table 1

Strains and plasmids used

Strain	Organism	Plasmid/Mutation	Citation
ME41	*P. chlororaphis* 200B-1	pME28/GFP-PhuZ	(Kraemer et al., 2012)
ME91	*P. chlororaphis* 200B-1	pME57/GFP-PhuZD303A	This paper
ME92	*P. chlororaphis* 200B-1	pME58/GFP-PhuZD305A	This paper
ME93	*P. chlororaphis* 200B-1	pME61/GFP-PhuZD303305A	This paper
ME102	*P. chlororaphis* 200B-1	pME62/GFP-PhuZR217A	This paper
ME103	*P. chlororaphis* 200B-1	pME63/GFP-PhuZR217D	This paper
ME104	*P. chlororaphis* 200B-1	pME64/GFP-PhuZD305R	This paper
ME105	*P. chlororaphis* 200B-1	pME65/GFP-PhuZR217DD305R	This paper